HHS Public Access

Author manuscript

*Phys Med Biol*. Author manuscript; available in PMC 2019 May 10.

Published in final edited form as:

*Phys Med Biol*. ; 63(10): 105001. doi:10.1088/1361-6560/aabe37.

# Multi-resolution Simulation of Focused Ultrasound Propagation through Ovine Skull from a Single-element Transducer

**Kyungho Yoon**[1], **Wonhye Lee**[1], **Phillip Croce**[1], **Amanda Cammalleri**[1], and **Seung-Schik Yoo**[1,*]

[1]Department of Radiology, Brigham and Women's Hospital, Harvard Medical School, Boston, MA, USA

## Abstract

Transcranial focused ultrasound (tFUS) is emerging as a non-invasive brain stimulation modality. Complicated interactions between acoustic pressure waves and osseous tissue introduce many challenges in the accurate targeting of an acoustic focus through the cranium. Image-guidance accompanied by a numerical simulation is desired to predict the intracranial acoustic propagation through the skull; however, such simulations typically demand heavy computation, which warrants an expedited processing method to provide on-site feedback for the user in guiding the acoustic focus to a particular brain region. In this paper, we present a multi-resolution simulation method based on the finite-difference time-domain (FDTD) formulation to model the transcranial propagation of acoustic waves from a single-element transducer (250 kHz). The multi-resolution approach improved computational efficiency by providing the flexibility in adjusting the spatial resolution. The simulation was also accelerated by utilizing parallelized computation through the graphic processing unit (GPU). To evaluate the accuracy of the method, we measured the actual acoustic fields through *ex vivo* sheep skulls with different sonication incident angles. The measured acoustic fields were compared to the simulation results in terms of focal location, dimensions, and pressure levels. The computational efficiency of the presented method was also assessed by comparing simulation speeds at various combinations of resolution grid settings. The multi-resolution grids consisting of 0.5 and 1.0 mm resolutions gave acceptable accuracy (under 3 mm in terms of focal position and dimension, less than 5% difference in peak pressure ratio) with a speed compatible with semi real-time user feedback (within 30 s). The proposed multi-resolution approach may serve as a novel tool for simulation-based guidance for tFUS applications.

### Keywords

Focused Ultrasound; Computer Simulation; FDTD; Multi-resolution; Graphic Processing Unit

[*]All the correspondence to: Seung-Schik Yoo, Ph.D., MBA, Department of Radiology, Brigham and Women's Hospital, Harvard Medical School, 75 Francis Street, Boston, MA 02115, yoo@bwh.harvard.edu.

The beta version of the program codes for the software, named 'SoundWave Rider', is available at https://yoonkh.weebly.com/software.html.

## 1. Introduction

Focused ultrasound (FUS) technique, in which acoustic pressure waves are delivered to a small and localized area in the body, has been widely used in the field of non-invasive therapeutic applications, such as thermal ablation (McDannold *et al.*, 1998; Tung *et al.*, 2006; McDannold *et al.*, 2006; Liu *et al.*, 2007; Coluccia *et al.*, 2014) and extracorporeal shockwave therapies (Madersbacher and Marberger, 2003; Bailey *et al.*, 2014). The accurate placement of the FUS focus to a targeted specific-region of tissue through bone poses significant challenges due to complicated interactions between acoustic waves and osseous tissue, such as absorption, refraction, and reflection (Konofagou *et al.*, 2001; Hynynen *et al.*, 2001; Pinton *et al.*, 2012). Transcranial application of FUS to the brain is particularly vulnerable to problems such as high energy loss through the cranium, poor focusing, and formation of extra foci (Deffieux and Konofagou, 2010; Kyriakou *et al.*, 2015; Jing *et al.*, 2012; Robertson *et al.*, 2017b).

The use of low fundamental frequency ultrasound (typically ≤ 1 MHz) (Clement *et al.*, 2005), much lower than the 1–15 MHz range used for clinical ultrasound imagers, helps to alleviate concerns over significant wave attenuation and refraction of acoustic energy through the skull. The use of a phased-array FUS transducer configuration (consists of > 500 ultrasound elements surrounding the head) and their independent actuation, combined with phase correction schemes *via* a time-reversal technique (Jing *et al.*, 2012; Chauvet *et al.*, 2013), compensates for acoustic aberration caused by the skull (Aubry *et al.*, 2003; Hynynen *et al.*, 2004). This method, combined with magnetic resonance (MR) guidance, has been utilized for thermal ablation of brain tumors and functional neurosurgery in humans through the use of high intensity FUS (HIFU), typically using a few hundred to thousand watts (Martin *et al.*, 2009; McDannold *et al.*, 2010; Elias *et al.*, 2013). The MR-guided transcranial FUS (tFUS) was also applied for temporary disruption of the blood brain barrier (BBB) using the concomitant vascular injection of microbubbles in animal models (Sheikov *et al.*, 2004; Hynynen *et al.*, 2006; Hynynen, 2008).

Single-element FUS transducer configurations, although lacking an aberration correction mechanism, have also been successfully implemented in transcranial applications by positioning the transducer over the scalp, being acoustically-coupled using water-containing bags, cones, or polymer hydrogels (Kim *et al.*, 2014; Lee *et al.*, 2015; Kim *et al.*, 2012b; Younan *et al.*, 2013). For example, FUS-mediated brain stimulation, utilizing the low-intensity pulsed ultrasound, has been demonstrated in small animals (Kim *et al.*, 2014; Yoo *et al.*, 2011; Kim *et al.*, 2015; Kim *et al.*, 2012b; Yoo *et al.*, 2017), sheep (Lee *et al.*, 2016c) and non-human primates (Deffieux *et al.*, 2013; Wattiez *et al.*, 2017), and in humans (Lee *et al.*, 2016b; Legon *et al.*, 2014; Lee *et al.*, 2015; Lee *et al.*, 2016a; Lee *et al.*, 2017). Single-element FUS transducers have also been used to study the disruption of the BBB in several animal models (McDannold *et al.*, 2008; Downs *et al.*, 2015; McDannold *et al.*, 2011).

A geometric derivation of the acoustic focal location and an acoustic intensity estimated from the simple application of attenuation factor in the acoustic path have been adopted (Kim *et al.*, 2012a; Lee *et al.*, 2016c; Lee *et al.*, 2015). These techniques are typically administered at a low-intensity under the threshold that can cause temperature changes or

pressure changes detectable by *in vivo* imaging techniques such as MR thermometry (Ishihara *et al.*, 1995; Yoo *et al.*, 2011) or acoustic radiation force imaging (ARFI) (Kaye *et al.*, 2011; Kennedy, 2005). Therefore, a separate mode of image-guidance/planning for the sonication is needed to accurately place the small and invisible acoustic focus to a specific region-of-interest, which may differ anatomically and functionally depending on individuals. To augment this process, a numerical simulation that estimates the location and intensity of the acoustic focus is desired for the accurate and quantifiable administration of tFUS (White *et al.*, 2006; Schwenke *et al.*, 2015).

Various numerical studies have been conducted to develop simulation methods to characterize the acoustic propagation during tFUS (Mueller *et al.*, 2017; Yin and Hynynen, 2005; Pulkkinen *et al.*, 2014; Baron *et al.*, 2009; Robertson *et al.*, 2017a; Pinton *et al.*, 2009). The finite element method (FEM) has been used to solve the wave equations to model the acoustic pressure propagation through the human cranium (Legon *et al.*, 2014), but it requires a computationally demanding process such as finding an inverse system matrix (Bathe, 2006). The finite-difference time-domain (FDTD) method greatly improves computational efficiency by progressively solving the pressure and velocity of sound waves that are discretized in both time and space domains (Taflove and Hagness, 2005), and is available through commercial and non-commercial software (Treeby and Cox, 2010; Kaufman *et al.*, 2008; Comsol, 2005). FDTD has been used to estimate the location and *in situ* pressure level of acoustic focus for BBB disruption (Deffieux and Konofagou, 2010), neuromodulation (Mueller *et al.*, 2017; Robertson *et al.*, 2017b), and sonothrombolysis (Baron *et al.*, 2009).

FDTD-based simulations are typically performed based on setting the simulation grid in a fixed spatial resolution (at the highest resolution possible) across an entire simulation volume. In the present study, we were motivated to examine the utility of employing a multi-resolution approach in FDTD to achieve a semi real-time simulation (for enabling on-line/on-site feedback) necessary to track/estimate the orientation and location of the acoustic focus from a single-element FUS transducer. Non-uniform grid (Jiang and Arai, 1998) can be alternatively used for providing a degree of flexibility in setting multiple resolutions, but it requires the spatial matching between adjacent grids at the interfaces that have different resolutions (Krumpholz and Katehi, 1996; Zhi *et al.*, 2013). Multi-resolution approaches are generally adopted to probe the spatially-restricted areas-of-interest and able to solve the wave propagation problem at the non-matching grid/node interfaces (Krumpholz and Katehi, 1996; Zhi *et al.*, 2013). The approaches have been utilized in expediting the data processing/acquisition, for example, in an optical geo-survey (van Lier *et al.*, 2009; Kurtz *et al.*, 2014) or in functional neuroimaging (Yoo *et al.*, 1999; Yoo *et al.*, 2001). We hypothesized that a similar multi-resolution approach is applicable to simulate the wave propagation when a single-element FUS transducer having a fixed focal length (*i.e.,* rough *a priori* information on the focal location is known) is used to sonicate a specific location of the brain. For example, a high spatial resolution grid is used to simulate wave propagation from the transducer to the focal areas (as a primary local region-of-interest) while sparse spatial sampling can be used to model the area outside without sacrificing the overall simulation quality.

To assess the accuracy and performance envelop (such as incident angle of sonication) of the proposed method, we conducted the FDTD-based acoustic simulation using different grid dimension settings (fixed- and multi-resolution approaches) to model FUS application through *ex vivo* sheep skull caps, and compared the results to the ones obtained from actual mapping of acoustic pressure using a hydrophone. We also performed the simulation using a closed sheep skull sample. The simulation was implemented in a graphic processing unit (GPU) environment with parallel processing capability to expedite the computation, and the resulting computational speed was compared to that from using a central processing unit (CPU).

## 2. Methods

### 2.1. Sheep skull preparation and CT data acquisition

All procedures for obtaining *ex vivo* sheep skulls were carried out in accordance with the ethical and safety rules set forth by a local Institutional Animal Care and Use Committee (IACUC). Five adult sheep (Dorset, all female, weight = 35.8 ± 6.1 kg) were euthanized, and a skull cap (having hexagonal shape over the brain, approximately 8 cm in anterior-posterior length and 6 cm in width right-left) was excised and fixated with 10% formalin for approximately one year. In two skulls (named ‘S1’ and ‘S2’ herein), effort was made to remove the periosteum and dura mater around the skull (by scraping the skull surface inside and out) using surgical scalpels and rongeurs (‘processed skull’ referred herein). The other three skulls (named ‘S3’, ‘S4’ and ‘S5’) had most of the soft tissue/skin remaining, preserving the overall tissue structures (*i.e.*, ‘intact skull’). A ceramic screw was implanted at the posterior edge of each skull to place a plastic applicator containing four donut-shaped fiducial markers (Pinpoint, Beekley Corp., Bristol, CT), which were later used for co-registration between the actual and virtual spaces of the skull phantom. A holder was connected to the applicator to rotate the skull with respect to the incident FUS beam (figure 1). The skull samples were preserved in degassed water for at least 24 h inside a vacuum chamber (Best Value Vacs, Naperville, IL) prior to acoustic mapping.

To obtain the geometric information of the sheep skull phantoms (being attached to the applicator), a three-dimensional (3D) computed tomography (CT) scan (Aquilion ONE, Toshiba, Japan) was conducted with an isotropic voxel of $0.5 \times 0.5 \times 0.5$ mm$^3$, covering the field-of-view (FOV) of $150 \times 125 \times 125$ mm$^3$. Due to the high degrees of individual variability in cranial structures (Lee *et al.*, 2015) and ultrasound propagation being sensitive to a specific skull geometry (Hynynen *et al.*, 2001; Konofagou *et al.*, 2001), a CT scan for each skull was necessary.

### 2.2. Characterization of acoustic field via hydrophone measurement

The schematics of the acoustic field measurement setup are illustrated in figure 1. The experiments were carried out in a water tank that contained degassed, distilled water. The pressure field was generated by a single-element FUS transducer (GPS200-400128, Ultran Group, Hoboken, NJ) whereby the acoustic waves generated by a piezoelectric disc are focused using a concave acoustic lens. The diameter/aperture ($D_t$) of the transducer was 37 mm and the focal length was 30 mm from the exit plane. The pulsed sinusoidal waves were

generated using a function waveform generator (33500B, Keysight, Santa Rosa, CA) operating at a frequency of 250 kHz, tone burst duration (TBD) of 100 μs at a 3% duty cycle. The generated sinusoidal waves (input peak-to-peak amplitude of 100 mV) were amplified (a linear power amplifier, 240L, Electronics and Innovations, Rochester, NY) and transmitted to the FUS transducer *via* an impedance matching box (JT-800, Electronics and Innovations, Rochester, NY). A plastic applicator holding the transducer had two fiducial markers to register its location and orientation with respect to the virtual simulation space.

The measurements were conducted by a needle-type hydrophone (HNR500, Onda, Sunnyvale, CA) attached to a three-axis robotic stage (Bi-Slides, Velmex, Bloomfield, NY) that shared the mutual spatial coordinates of the transducer. The center lines of the transducer and hydrophone were aligned using the robotic stage, and each of the prepared skulls were placed between the transducer and hydrophone so that the wave front met the skull surface as perpendicular as possible. The distance between the skull and the transducer exit plane was 5.1 ± 0.2 mm ($n$ = 5 skulls). The acoustic pressure field was measured in three planes that were longitudinal and perpendicular to the FUS transducer (see figure 1 for the illustration of the axis), *i.e.*, YZ-plane (ΔY = 21 mm, ΔZ = 41 mm, Δm = 1 mm at D = 20 mm), XZ-plane (ΔX = 21 mm, ΔZ = 41 mm, Δm = 1 mm at D = 20 mm), XY-plane (ΔX = 21 mm, ΔY = 21 mm, Δm = 1 mm at D = 30 mm) where ΔX, ΔY, ΔZ are respectively the x, y, z-directional length of the scanning plane, Δm is the measuring interval, and D indicates the distance between the hydrophone tip and the exit plane of the transducer. At each coordinate, the value from averaged hydrophone readings was used in the acoustic mapping ($n$ = 32 measurements). We also increased the TBD up to 10 ms to examine the presence of reverberations or interference that could occur at longer sonication durations ($n$ = 2 skulls), and found that the use of a long TBD did not alter the measured pressure values. Therefore, we kept the TBD of 100 μs for all the measurements to expedite the mapping procedure. With nine varying incident angles of FUS beam (*i.e.*, 0°, x±10°, x±15°, y±10°, y ±15°) with respect to the normal skull surface at the geometric entry point, a total of 27 acoustic field maps were generated for each of the skull phantoms covering three planes.

### 2.3. Co-registration between the actual and simulation spaces

The co-registration between the actual measurement space and the virtual simulation space was performed through optical-based position-tracking whereby the detailed protocol can be found elsewhere (West and Maurer, 2004; Kim *et al.*, 2012a; Lee *et al.*, 2015). Briefly, the spatial coordinates of the four fiducial markers were obtained from the virtual simulation coordinate system (*i.e.*, the acquired CT data), and registered to the actual space using an optical tracking system (Polaris Vicra and NDI Tool Track, Northern Digital Inc., Ontario, Canada) (figure 1). Subsequently, the coordinate transformation equation between the two coordinate systems was derived using a point-based rigid body registration method (Fitzpatrick *et al.*, 1998; Moghari and Abolmaesumi, 2007; Pietrzyk *et al.*, 1994). The location and orientation of the FUS transducer (represented as a center position and its normal vector) was found by collecting the spatial coordinates from two fiducial markers on the transducer applicator.

Through the above procedure, we co-registered nine sets of sonication angles (0°, x±10°, x ±15°, y±10°, and y±15° from the normal vector to the skull surface) for respective skull phantoms (a total of 45 registrations were conducted; 9 angles × 5 skulls). The registration error, in terms of root-mean-square (RMS) distance, between the actual and registered coordinates of the four fiducial markers was less than 1 mm for each angle condition and skull phantom (0.41 ± 0.15 mm, across 45 registrations).

### 2.4. Simulation hardware

We implemented a FDTD formulation and the corresponding multi-resolution simulation approach through parallel computation utilizing a GPU device, with the aim of semi-real time feedback for the operators. The simulation was performed using a quad-core work station (Intel(R) Core(TM) i7-7700 CPU @ 3.60 GHz, 64 GB memory, Microsoft Windows 10 64bit) and GPU device (Nvidia's single Pascal card, GeForce GTX 1080, 2560 cores, 8 GB GDDR5X memory @ 320 GB/s bandwidth). The computational implementation was written in CUDA (Nvidia, Santa Clara, CA) and C++ languages.

### 2.5. FDTD formulation

We used the second-order Westervelt-Lighthill equation (Westervelt, 1957; Lighthill, 1978; Jing *et al.*, 2011) to mathematically define the mechanical pressure wave propagation through the media,

$$\nabla^2 p - \frac{1}{c^2}\frac{\partial^2 p}{\partial t^2} + \frac{\delta}{c^4}\frac{\partial^3 p}{\partial t^3} + \frac{\beta}{\rho c^4}\frac{\partial^2 p^2}{\partial t^2} = 0, \quad (1)$$

where $p$ is the acoustic pressure, $c$ is the ultrasound speed, $t$ is the time, $\delta$ is the ultrasound diffusivity, and $\beta$ is the nonlinearity coefficient (which governs wave attenuations through media). The equation is suitable for solving nonlinear phenomena such as sound wave propagation through materials with variable shear and bulk viscosity (*e.g.,* skulls) (Solovchuk *et al.*, 2013).

To replace nonlinear terms, which may decrease computational efficiency, we used the linearized version of Westervelt-Lighthill equation as a governing equation (Liebler *et al.*, 2004; Kyriakou *et al.*, 2015),

$$\nabla^2 p - \frac{1}{c^2}\frac{\partial^2 p}{\partial t^2} - \frac{\tilde{a}}{c^2}\frac{\partial p}{\partial t} = 0 \text{ with } \tilde{a} = 2a\sqrt{\frac{a^2 c^4}{4\pi^2 f^2} + c^2}, \quad (2)$$

in which $a$ is the attenuation coefficient of the medium and $f$ is the fundamental frequency of the ultrasound.

By employing the staggered FDTD algorithm (Taflove and Hagness, 2005; Pinton *et al.*, 2009), the pressure and velocity field was discretized as,

$$
\begin{aligned}
{}^{t+\Delta t}P_{i,j,k} &= {}^{t}P_{i,j,k} - C^{p}_{i,j,k}\Big[({}^{t+1/2\Delta t}V^{x}_{i,j,k} - {}^{t+1/2\Delta t}V^{x}_{i-1,j,k}) + \\
&({}^{t+1/2\Delta t}V^{y}_{i,j,k} - {}^{t+1/2\Delta t}V^{y}_{i,j-1,k}) + ({}^{t+1/2\Delta t}V^{z}_{i,j,k} \\
&- {}^{t+1/2\Delta t}V^{z}_{i,j-1,k})\Big] - A_{i,j,k}\,{}^{t}P_{i,j,k}, \\
{}^{t+1/2\Delta t}V^{x}_{i,j,k} &= {}^{t-1/2\Delta t}V^{x}_{i,j,k} - C^{vx}_{i,j,k}\Big[{}^{t}P_{i+1,j,k} - {}^{t}P_{i,j,k}\Big], \\
{}^{t+1/2\Delta t}V^{y}_{i,j,k} &= {}^{t-1/2\Delta t}V^{y}_{i,j,k} - C^{vy}_{i,j,k}\Big[{}^{t}P_{i,j+1,k} - {}^{t}P_{i,j,k}\Big], \\
{}^{t+1/2\Delta t}V^{z}_{i,j,k} &= {}^{t-1/2\Delta t}V^{z}_{i,j,k} - C^{vz}_{i,j,k}\Big[{}^{t}P_{i,j,k+1} - {}^{t}P_{i,j,k}\Big], \\
\text{with } C^{p}_{i,j,k} &= \rho_{i,j,k}c^{2}_{i,j,k}\frac{\Delta t}{\Delta s},\ A_{i,j,k} = 2\Delta t a_{i,j,k}\sqrt{\frac{a^{2}_{i,j,k}c^{4}_{i,j,k}}{4\pi^{2}f^{2}} + c^{2}_{i,j,k}} \\
\text{and } C^{vx}_{i,j,k} &= \frac{2}{\rho_{i,j,k} + \rho_{i+1,j,k}}\frac{\Delta t}{\Delta s},\ C^{vy}_{i,j,k} = \frac{2}{\rho_{i,j,k} + \rho_{i,j+1,k}}\frac{\Delta t}{\Delta s},\ C^{vz}_{i,j,k} \\
&= \frac{2}{\rho_{i,j,k} + \rho_{i,j,k+1}}\frac{\Delta t}{\Delta s},
\end{aligned}
\tag{3}
$$

where ${}^{t}P_{i,j,k}$ is the nodal pressure value, and each of ${}^{t}V^{x}_{i,j,k}$, ${}^{t}V^{y}_{i,j,k}$ and ${}^{t}V^{z}_{i,j,k}$ denotes the nodal wave velocity values from $x$, $y$, $z$ coordinates at time $t$. $c_{i,j,k}$, $\rho_{i,j,k}$, and $a_{i,j,k}$ are ultrasound speed, density, and attenuation coefficient of the corresponding media in the discretized domain ($i$, $j$, and $k$ are nodal indices), respectively. $\Delta t$ is the time interval, and $\Delta s$ is the discretized spatial interval.

The graphical illustration of staggered grids for estimating the nodal pressure and velocity is shown in figure 2. The propagation of the ultrasound was obtained by iteratively evaluating equation (3) for each time step until reaching the desired simulation time.

In general, the algorithm that solves explicit dynamic processes, including FDTD, may become spurious and non-physically diverse due to numerical error (Namiki, 2000; Noh and Bathe, 2013). Hence, it is essential in FDTD analysis to satisfy the stability condition called Courant-Friedrichs-Lewy (CFL) criterion which is written as the following equation (4) in 3D cases:

$$\Delta t \leq \frac{\Delta s}{\sqrt{3}c}. \tag{4}$$

### 2.6. Multi-resolution approach

The framework of the multi-resolution analysis consists of interconnecting the nodal pressure and velocity values (obtained according to equation (3) at the respective time step) between different resolution configurations. To use the FDTD in the context of the multi-resolution approach, we adopted the use of sequence of nested grids, $L^{(i)}$ ($i$ is the index for the grid level) having different resolutions (see figure 3 for the example of 2-level, multi-resolution grids; $i = 1$ for the global grid and $i = 2$ for the local grid).

The pressure and velocity at nodes in the respective grids were analyzed by equation (3), and these values were bridged between different resolution grids (*i.e.*, local and global) using a set of two interaction equations (6) and (7). For convenience of algebraic manipulation, we defined the vector form of the nodal pressure and velocity values defined in the respective grids $L^{(i)}$, as represented in equation (5).

$$
\begin{aligned}
{}^{t}\mathbf{P}^{(i)} &= \left[ {}^{t}P^{(i)}_{1,1,1} \;\; {}^{t}P^{(i)}_{2,1,1} \;\cdots\; {}^{t}P^{(i)}_{n_x,n_y,n_z} \right]^{T}, \\
{}^{t+1/2\Delta t}\mathbf{V}^{x(i)} &= \left[ {}^{t+1/2\Delta t}V^{x(i)}_{1,1,1} \;\; {}^{t+1/2\Delta t}V^{x(i)}_{2,1,1} \;\cdots\; {}^{t+1/2\Delta t}V^{x(i)}_{n_x,n_y,n_z} \right]^{T}, \\
{}^{t+1/2\Delta t}\mathbf{V}^{y(i)} &= \left[ {}^{t+1/2\Delta t}V^{y(i)}_{1,1,1} \;\; {}^{t+1/2\Delta t}V^{y(i)}_{2,1,1} \;\cdots\; {}^{t+1/2\Delta t}V^{y(i)}_{n_x,n_y,n_z} \right]^{T}, \\
{}^{t+1/2\Delta t}\mathbf{V}^{z(i)} &= \left[ {}^{t+1/2\Delta t}V^{z(i)}_{1,1,1} \;\; {}^{t+1/2\Delta t}V^{z(i)}_{2,1,1} \;\cdots\; {}^{t+1/2\Delta t}V^{z(i)}_{n_x,n_y,n_z} \right]^{T}.
\end{aligned}
\tag{5}
$$

The following interaction equation (6) was used for updating pressure values from the high-resolution local nodes to the low-resolution global nodes.

$$
{}^{t}P^{(i)}_{i,j,k} = \sum_{l=1}^{8} \left[ W^{(i+1),l}_{i,j,k} \mathbf{B}^{(i+1),l}_{i,j,k} \right] {}^{t}\mathbf{P}^{(i+1)} \text{ in } L^{(i+1)}, \tag{6}
$$

in which $W^{(i+1),l}_{i,j,k}$ is the trilinear interpolation weight (Bathe, 2006) for evaluating the global nodal pressure values ( ${}^{t}P^{(i)}_{i,j,k}$) from the local nodal pressure values ( ${}^{t}P^{(i+1)}_{i,j,k}$), and $\mathbf{B}^{(i+1),l}_{i,j,k}$ is the Boolean vector for connecting the local nodes to the corresponding global nodes.

Likewise, nodal velocity values were updated using equation (7) by evaluating the interaction equation on the interface between the low-resolution global nodes and the high-resolution local nodes,

$$
\begin{aligned}
{}^{t+1/2\Delta t}V_{i,j,k}^{x(i+1)} &= \sum_{l=1}^{4}\left[\overline{W}_{i,j,k}^{(i),l}\overline{\mathbf{B}}_{i,j,k}^{(i),l}\right]{}^{t+1/2\Delta t}\mathbf{V}^{x(i)} \quad \text{on } S^{(i)}, \qquad (7)\\
{}^{t+1/2\Delta t}V_{i,j,k}^{y(i+1)} &= \sum_{l=1}^{4}\left[\overline{W}_{i,j,k}^{(i),l}\overline{\mathbf{B}}_{i,j,k}^{(i),l}\right]{}^{t+1/2\Delta t}\mathbf{V}^{y(i)} \quad \text{on } S^{(i)},\\
{}^{t+1/2\Delta t}V_{i,j,k}^{z(i+1)} &= \sum_{l=1}^{4}\left[\overline{W}_{i,j,k}^{(i),l}\overline{\mathbf{B}}_{i,j,k}^{(i),l}\right]{}^{t+1/2\Delta t}\mathbf{V}^{z(i)} \quad \text{on } S^{(i)},
\end{aligned}
$$

where $\overline{W}_{i,j,k}^{(i),l}$ is the bilinear interpolation weight (Bathe, 2006) for evaluating the local nodal velocity values ( ${}^{t+1/2\Delta t}V_{i,j,k}^{x(i+1)}$, ${}^{t+1/2\Delta t}V_{i,j,k}^{y(i+1)}$, ${}^{t+1/2\Delta t}V_{i,j,k}^{z(i+1)}$) from the global nodal velocity values ( ${}^{t+1/2\Delta t}V_{i,j,k}^{x(i)}$, ${}^{t+1/2\Delta t}V_{i,j,k}^{y(i)}$, ${}^{t+1/2\Delta t}V_{i,j,k}^{z(i)}$), $\overline{\mathbf{B}}_{i,j,k}^{(i),l}$ is the Boolean vector for connecting the global nodes to the corresponding local nodes, and $S^{(i)}$ is the interface between $L^{(i)}$ and $L^{(i+1)}$. A conceptual description of the process is shown in figure 3.

## 2.7. Transducer modeling

Accurate representation of the acoustic source is an important part of tFUS simulation. The FUS transducer used in the present study consisted of a piezoelectric disc and an acoustic lens material (figure 4). Ultrasound waves generated from the piezoelectric disc yielded different phase and attenuation of the waves when exiting the source surface due to the curvature of the lens. To model the semi-spherical shape of the acoustic lens, we used a discrete source model (Martin *et al.*, 2016) having a diameter ($D_t$) of 37 mm and a radius of curvature ($\kappa$) of 20 mm. At the determined source position, we substituted the pressure input values using the following equation (8):

$$
P_{source} = \alpha A_0 \sin(2\pi f t - \Delta\varphi) \text{ with } \Delta\varphi = \frac{2\pi d}{\lambda} \text{ and } \alpha = e^{-a_{tr} df}, \qquad (8)
$$

where $\alpha$ is attenuation ratio, $A_0$ is amplitude of ultrasound, $\Delta\varphi$ is phase difference, $f$ is operating frequency, $t$ is time, $\lambda$ is wavelength of the ultrasound, $a_{tr}$ is an attenuation coefficient, and $d$ is wave travel distance from the piezoelectric disc to the source surface geometry. Considering the specification of actual transducer lens material (Ultem 1000, SABIC Innovative Plastics, Burkville, AL), we used the parameters of $f$ = 250 kHz, $\lambda$ = 9.61 mm (derived from (Sheen *et al.*, 1997)) and $a_{tr}$ = 164 Np·m$^{-1}$·MHz$^{-1}$ from actual measurements on a same material (at 250 kHz) in equation (8).

## 2.8. Preparation of skull CT data and parameter assignment for simulation

The acquired CT images were resampled to isotropic voxels (1.0 × 1.0 × 1.0 mm$^3$ and 2.0 × 2.0 × 2.0 mm$^3$) using Lanczos filter algorithm (Burger and Burge, 2009) for constructing various resolution grids. Because the CT data was acquired at 0.5 mm isotropic voxel, the highest resolution for the simulation was set at 0.5 mm in an isotropic grid. To describe the

porous and inhomogeneous characteristics of the skulls, we evaluated the normalized CT intensity map $\phi_{i,j,k}$ ($0 \leq \phi_{i,j,k} \leq 1$) without any thresholding. Due to the presence of the large deviations in the simulation result (in terms of the acoustic pressure) from two 'processed' skulls ('S1' and 'S2'; data not shown), intensity threshold (average 48% from the maximum) was applied to 'S1' and 'S2' for segmenting osseous structure from the CT volumetric data.

Acoustic parameters, material density ($\rho_{i,j,k}$), wave speed ($c_{i,j,k}$), and attenuation factors ($a_{i,j,k}$), were represented as following equation (9);

$$\begin{aligned} \rho_{i,j,k} &= \rho_{water} + (\rho_{skull} - \rho_{water})\phi_{i,j,k}, \\ c_{i,j,k} &= c_{water} + (c_{skull} - c_{water})\phi_{i,j,k}, \\ a_{i,j,k} &= a_{water} + (a_{skull} - a_{water})\phi_{i,j,k}, \end{aligned} \quad (9)$$

in which $\rho_{skull}$ is the density of the skull, $\rho_{water}$ is the density of water, $c_{skull}$ is the ultrasound speed in the skull, $c_{water}$ is the ultrasound speed in water, $a_{skull}$ is the attenuation coefficient of the skull, and $a_{water}$ is the attenuation coefficient of water. We used the acoustic properties, $\rho_{skull}$ = 2,200 kg/m$^3$, $\rho_{water}$ = 1,000 kg/m$^3$, $c_{skull}$ = 2,800 m/s, $c_{water}$ = 1,500 m/s, $a_{skull}$ = 20 Np·m$^{-1}$, and $a_{water}$ = 0 Np·m$^{-1}$ (Goss *et al.*, 1979; Fry and Barger, 1978; Kyriakou *et al.*, 2015; Deffieux and Konofagou, 2010). The linear scaling of the wave speed and attenuation factor with respect to the bone density was applied according to the work by Evans and Tavakoli (1990).

### 2.9. Preparation of various resolution grids for simulation

We constructed a total of six different virtual simulation spaces, each with a different combination of resolution grids. Three of them utilize the fixed grid resolutions and the other three are based on the multi-resolution approach. The detailed size of the resolution grid, the number of matrices, their node numbers, and the size of the physical field are all tabulated in table 1. The spatial resolutions of 0.5 mm, 1.0 mm, and 2.0 mm correspond to 1/12, 1/6, and 1/3 of the wavelength ($\lambda$) at frequency of 250 kHz in the water, respectively. The graphical depiction of the grid settings is illustrated in figure 5. Two levels of global and local grid settings were used for the multi-resolution simulation. The higher resolution was assigned to the local grid volume that includes (1) transducer, (2) skull, and (3) geometric focal point while the global grid was assigned to the volume that surrounds the local grid.

### 2.10. Measures for evaluating the simulation results

Following the CFL criterion in equation (4) ($\Delta t \leq 0.1$ μs for 0.5 mm resolution, $\Delta t \leq 0.2$ μs for 1.0 mm resolution, $\Delta t \leq 0.4$ μs for 2.0 mm resolution), all simulations were conducted with a discretized time interval of $\Delta t$ = 0.05 μs (sufficiently conforms to the criteria across all the resolution conditions) and 1,200 incremental steps, covering physical time of 60 μs (= 0.05 μs × 1,200 time steps). The use of a 60 μs time window was sufficient for observing the initial formation of the focus, which also shared the similarity to the actual field mapping (100 μs). From the simulation results, we evaluated acoustic pressure fields on YZ-, XZ-, XY-planes in the same location as the actual measurement.

Three physical quantities—(1) the spatial location of the focus, (2) the dimension of the focus (length and width of the ellipsoidal focus), and (3) the pressure peak ratio at the focus, were separately measured from the respective simulation planes and were compared to the results obtained from the actual measurement. In more detail, the spatial location of the focus ( $c_1^{ij}, c_2^{ij}$) was defined as the center of the focal area at 90%-maximum (denoted as $A_{90\%}$) in which the index $ij$ represents the respective planes (*i.e.*, $ij \in$ {YZ, XZ, XY}). A higher threshold, as opposed to the conventional full-width-at-half-maximum (FWHM) for the area definition, was applied to closely estimate the areas of neuromodulatory effects (Kim *et al.*, 2013 and Kim *et al.*, 2014). The dimension of the focus, measured in terms of length $l^{ij}$ and width $w^{ij}$, was also evaluated on the $A_{90\%}$. The pressure peak ratio $R^{ij}$ was defined as the ratio of the peak pressure after the transcranial application to the peak pressure which was measured in the absence of skull. Since the actual pressure output from the transducer varies according to the electrical input/amplification/impedance matching, the derivation of the ratio $R^{ij}$ was used, instead of absolute pressure values, in evaluating the performance of simulation. All the quantities obtained from simulation results are noted by upper bar on the corresponding symbols ( $\bar{c}_1^{ij}$, $\bar{c}_2^{ij}$, $\bar{l}^{ij}$, $\bar{w}^{ij}$, and $\bar{R}^{ij}$). The example from one skull sample ('S3') is shown in figure 6.

The difference between the actual measurement and simulation results was represented by the following performance indices, in terms of location of focus ($\Delta_F$), length ($\Delta_l$), width ($\Delta_w$), and peak ratio ($\Delta_{PR}$) to quantify the accuracy of the simulation:

$$\Delta_F = \sqrt{\left(c_1^{ij} - \bar{c}_2^{ij}\right)^2 + \left(c_2^{ij} - \bar{c}_2^{ij}\right)^2}, \tag{10}$$

$$\Delta_l = \left|l^{ij} - \bar{l}^{ij}\right| \text{and } \Delta_w = \left|w^{ij} - \bar{w}^{ij}\right|,$$

$$\Delta_{PR} = \frac{\left|R^{ij} - \bar{R}^{ij}\right|}{R^{ij}} \text{ with } ij \in \left\{\text{YZ, XZ, XY}\right\}.$$

## 2.11. Simulation setting for a closed skull sample

We further applied the multi-resolution simulation approach to model the soundwave propagation inside the closed cranial cavity. An ovine skull (Skulls Unlimited, Oklahoma City, OK) was purchased and underwent the same procedure (*i.e.*, application of a plastic applicator containing fiducial markers and acquisition of CT) to obtain information on the skull geometry. The location of the FUS transducer was maneuvered to place the focus near the left side of the somatosensory area. For the numerical simulation, the discretized time interval ($\Delta t$ = 0.05 μs; as same as *ex vivo* skull samples) was used, but the simulated physical time was doubled (2,400 incremental steps, therefore, 120 μs) to observe the effects of prolonged wave propagations within the skull. The simulation time of 120 μs allows for reasonable observation of the possible formation of standing wave whereby the incident wave front passes through the focal region approximately four times (inner diameter of the skull cavity was ~50 mm). To compensate for increased computational load accompanying

the longer simulation time, the physical field size was adjusted to fit the size of the skull as close as possible (on the order of 100 × 150 × 125 $mm^3$; reducing the number of nodes for the simulation; *i.e.*, the processing time). The simulation accuracy is not affected by the chosen field size as long as the field contains the main areas-of-interest for wave propagation. The detailed specification of the simulation grids were tabulated in table 2.

## 3. Results

### 3.1. Qualitative evaluation of the overall accuracy at highest grid resolution ('0.5 mm grid')

Prior to evaluating the efficacy of the multi-resolution approach, simulation results obtained from the highest spatial resolution setting (fixed '0.5 mm grid') were evaluated with respect to those obtained from the actual measurements across four performance indices, *i.e.*, differences in focal position ($\Delta_F$), in focal dimension (length and width, $\Delta_l$ and $\Delta_w$ respectively), and in peak pressure ratio ($\Delta_{PR}$). The results were further divided into two sub-groups, (1) data from the processed skulls (having the soft tissue removed, *i.e.*, 'S1' and 'S2', named Case A in table 3), and (2) the same data sets obtained from the intact skulls ('S3', 'S4', and 'S5', Case B in table 3). The detailed individual data is given in the Supplemental Data (see tables A1–A3).

We found that the results acquired from the intact skull (Case B in table 3) yielded smaller differences in terms of focal position ($\Delta_F$: 1.3–1.6 mm), compared to the measurements from the processed skulls (Case A, 2.7–4.4 mm). A similar trend was observed from the perspective of differences in focal dimension ($\Delta_l$ and $\Delta_w$, table 3), and in peak pressure level ($\Delta_{PR}$: 5.2–6.3% from the intact skulls compared to the 8.3–10.1% in processed skulls, table 3).

To examine the effects of incident angle in regards to the skull surface on simulation quality, we derived the performance indices from the three intact skull phantoms ('S3', 'S4', and 'S5') at a reduced range of sonication angles (0°, x±10° and y±10°: Case C in table 3). The effect of the narrowing incident sonication angle yielded smaller differences in focal position and dimensions (most of them become less than 1 mm). This restriction of the sonication angle yielded better approximation of the pressure ($\Delta_{PR}$) compared to Case B (all angle condition), being closer to the actual measured value (less than 5% averaged differences).

### 3.2. Evaluation of the multi-resolution approach in estimating the focal location/dimension/pressure level

We compared the accuracy and computational cost in numerical simulations using different resolution grids including the use of multi-resolution grids. After determining the effects from the choice of skull samples and the range of incident sonication angles, simulations in this section were performed only on the intact skulls at the incident angles covering up to ±10°. The simulation performance was assessed using the same set of performance indices ($\Delta_F$, $\Delta_l$, $\Delta_w$ and $\Delta_{PR}$) and the computational time. The detailed comparison data was given in the Supplemental Data (see tables A4–A15), while the summary of the results was tabulated in table 4.

In terms of difference in focal position ($\Delta_F$) compared to the actual measurement, the results obtained from the use of '0.5 mm grid' showed the smallest difference (1.2–1.4 mm) among the simulation settings. The use of '1.0 mm grid' increased the $\Delta_F$ slightly compared to the use of '0.5 mm grid' (*e.g.*, 1.7–2.4 mm); however, the use of '2.0 mm grid' markedly increased the $\Delta_F$ to 7.8–8.9 mm. In multi-resolution approaches involving 0.5 mm grid setting in the local grid (*i.e.*, '0.5&1.0 mm grids' and '0.5&2.0 mm grids'), $\Delta_F$ was almost identical to the result from the use of '0.5 mm grid' (*i.e.*, less than 1.5 mm in difference). On the other hand, the use of '1.0&2.0 mm grids', resulted in slightly higher $\Delta_F$ (*e.g.*, 1.7–2.3 mm), resembling the results obtained from using '1.0 mm grid'.

Regarding the differences in focal dimension (represented in $\Delta_l$ and $\Delta_w$), the use of '1.0 mm grid' generated comparable results to those from the use of '0.5 mm grid'. The use of '2.0 mm grid', however, yielded much greater differences, more than a six-fold increase in the focal size compared to the use of '0.5 mm grid'. All other multi-resolution settings, on the other hand, generated similar degrees of differences in focal dimension compared to those from using '0.5 mm grid'.

The difference in peak pressure ratio ($\Delta_{PR}$), measured from the use of '1.0 mm grid' (3.2–6.9%), was comparable to that of using '0.5 mm grid' (3.1–4.9%). The use of '2.0 mm grid' generated greater differences (on the order of 3–4 times, 20.7–47.7%) compared to the use of a smaller grid size. Multi-resolution simulation, performed using '0.5&1.0 mm grids' or '0.5&2.0 mm grids' settings, generated $\Delta_{PR}$ values similar to the values obtained at '0.5 mm grid', showing less than 5% in $\Delta_{PR}$. The use of '1.0&2.0 mm grids' yielded slightly higher $\Delta_{PR}$ (3.5–7.5%; table 4) than the use of '1.0 mm grid', but it was far smaller than the use of '2.0 mm grid'.

The computational time measured from using '0.5 mm grid' was 63 s. It was even further decreased to 8 s in the use of '1.0 mm grid' and 1 s in the use of '2.0 mm grid' (table 4). In the multi-resolution simulations, 30 s and 21 s was measured for completing the stimulations using '0.5&1.0 mm grids' and '0.5&2.0 mm grids', respectively. We also performed an additional simulation with '0.5 mm grid' by using only a single core CPU on the same computer hardware platform to evaluate efficacy of GPU multi-threading process, and the simulation took 1,421 s.

### 3.3. Evaluation of multi-resolution approach in a closed skull sample

The simulation results (illustrated in figure 7 and table 5) were expressed in terms of pressure distribution, computational time, the differences in pressure peak ratio ($\Delta_{PR}$), and focal position ($\Delta_F$) with respect to the results obtained from the highest spatial resolution setting (*i.e.*, fixed '0.5 mm grid'; figure 7(a)). From the analysis of the '0.5 mm grid' setting, unlike the open skull example, signs of reverberations (a formation of multiple local maximum pressures along the acoustic pathway) were evident as well as the presence of high pressure level near the floor of the skull (marked by the arrow; figure 7(a)). The processing time was 107 s in this setting. The use of '1.0 mm grid' setting captured many of these features but showed difference of 11.3 mm in terms of focal position ($\Delta_F$) and 8.5% $\Delta_{PR}$ (figure 7(b)). In '2.0 mm grid', although the simulation was quick (1 s), the pressure map became vastly different from the ones used in the higher resolution grid, with increased

differences of $\Delta_F$ = 12.3 mm and $\Delta_{PR}$ = 28.8% (figure 8(c)). The multi-resolution approach of '0.5&1.0 mm grids' setting showed a similar acoustic map to that of the '0.5 mm grid' setting (figure 7(d)), and gave comparable accuracy ($\Delta_F$ = 0.5 mm and $\Delta_{PR}$ = 1.7%) to the '0.5 mm grid' setting, but with reduced processing time (36 s). The use of '0.5&2.0 mm grids' (figure 7(e)) and '1.0&2.0 mm grids' (figure 7(f)), on the other hand, started to deviate from the above pressure distribution in both local and global grids, with marked increase in both $\Delta_F$ and $\Delta_{PR}$.

## 4. Discussion

The neuromodulatory potentials of tFUS, with its non-invasiveness, spatial specificity, and penetrability into the deep brain regions, may provide unique therapeutic applications for addressing various neurological and psychiatric disorders. Due to the use of low-intensity ultrasound that is evasive to *in vivo* detection, computer-based, on-site simulation of transcranial acoustic propagation becomes a desired feature in guiding the acoustic focus to a specific brain region-of-interest. In this study, we presented a multi-resolution FDTD simulation approach to model the transcranial acoustic wave propagation generated by a single-element FUS transducer using an ovine skull model. Our multi-resolution approach using GPU-based parallel processing allowed for simulation within 30 s, while achieving simulation accuracy under 3 mm in focal position and dimension, and less than 5% difference in peak pressure ratio (when compared to the actual acoustic mapping). The implementation made a vast improvement over the use of a single-CPU environment which took a much longer time (1,421 s), and is capable of providing semi-real time feedback guidance for tFUS applications.

We prepared *ex vivo* ovine skulls in two different conditions, *i.e.,* dividing them to 'processed' and 'intact' skulls, and evaluated their effects on the simulation quality. The simulations using intact, unprocessed skulls (Case B in table 3) generated more accurate estimations compared to the simulations using processed skulls (Case A in table 3) across the location/dimension of the focus and its pressure level. Our results suggest that the use of intact skulls is more appropriate to examine the transcranial transmission of ultrasound. This finding was puzzling, because we initially anticipated that removal of the soft tissue, by reducing tissue inhomogeneity, would yield a more accurate prediction from the simulation. Although we could not isolate the definite causes for the findings, we hypothesized that the mechanical means used for the removal of soft tissue (the periosteum or dura mater) might have introduced additional structural changes (*e.g.*, dents/damages to the skull surface) that cannot be properly characterized by the numerical simulation. Further investigation is necessary, for example, to evaluate the effects from different methods for skull preparation.

Numerical modeling of the cranial structure was also an important factor in the tFUS simulation. The cranium has two main structural features, a dense solid (compact bone) and a porous network of cancellous bone/trabeculae (Fellah *et al.*, 2004), each having different acoustic properties (*i.e.,* density and wave speed). FDTD offers an efficient method for analyzing wave propagation in an orthogonal grid setting; however, complicated skull geometry or interfaces between the trabeculae and inner/outer compact bone, would require

increased number of nodes/finer grids for their proper spatial description (Yu and Chen, 2009).

Since it is difficult to assign a single acoustic property to model the highly-inhomogeneous cancellous bone, we used variable acoustic properties based on the interpolation of a CT intensity map, as shown in equation (9). Due to the use of low frequency in the present work (*i.e.*, 250 kHz), relatively long wavelength (on the order of 6 mm) is less likely to interact with the heterogeneous diploë (trabeculae) in the skull (Deffieux and Konofagou, 2010). On the other hand, a previous study by Aubry and colleagues (Aubry *et al.*, 2003) suggested that the heterogeneous structure of the skull, such as diploë, can yield higher attenuation compared to the (more dense) compact bone. We note that accurate modeling of attenuation coefficient for the transcranial propagation of ultrasound has been challenging due to the presence of complicated acoustic interactions, such as mode conversion and backscattering (Marquet *et al.*, 2009; Pinton *et al.*, 2012). In addition, the spatial resolution of cranial CT data may insufficiently characterize the wave propagation through the complicated microstructure of the diploë (Marquet *et al.*, 2009; Pinton *et al.*, 2012). Further investigation is necessary to identify the unequivocal method for the proper assignment of CT-based cranial information to acoustic simulation parameters.

This interpolation method (in equation (9)) favored the use of high spatial resolution grid in modelling the skull structures (‘0.5 mm grid’ to results in good accuracy), but was computationally demanding. Biot’s theory (Fellah *et al.*, 2004; Lee *et al.*, 2007; Hosokawa, 2005) or the use of a grid (mesh) free method (Ala *et al.*, 2006; Yu and Chen, 2009; Liu and Liu, 2003) can be adopted to represent acoustic properties in a porous medium having complicated geometry, and warrants future investigation. We also note that the present simulation did not account for the presence of gray and white matter structures of brain, and inclusion of realistic brain tissues and their material characteristics would be conducive to increasing the overall accuracy of the acoustic simulation.

Based on the analysis of the simulation performance at the grid resolution of 0.5 mm, we found that the use of a sonication angle of ±15° (away from the normal vector to the skull surface) generated more error in estimating the focal location and the pressure level from the actual measurement (in table 3). The simulation showed an acceptable level of accuracy within 10° incident angles (less than 2 mm difference of focal location and less than 5% difference of peak pressure ratio compared to the actual mapping results). We conjectured that tFUS administration with an incident angle greater than 10° started to introduce mode conversion that could not be properly described in the present simulation models (White *et al.*, 2006; Marquet *et al.*, 2009; Pinton *et al.*, 2012). The highly-convoluted inner surface of the ovine skulls (having short-radius curvatures), in conjunction with insufficient CT image resolution to reflect this geometry, might have contributed to the findings. For the actual implementation of the current simulation settings in ovine model, therefore, the operator may need to keep the incident angle as perpendicular as possible to the skull surface (within 10°) for accuracy. Further investigation is necessary to probe source for the departure in simulation accuracy affected by the range of incident angles.

Accuracy and computational cost in different simulation resolution settings were also investigated (the results are shown in table 4). The use of '0.5 mm grid' would not be applicable for semi real-time guidance due to its long computational time (63 s). The use of '2.0 mm grid' expedited the simulation to mere 1 s, but with a sacrifice in the accuracy of modeling. The '1.0 mm grid' setting, on the other hand, generated significantly higher performance while showing excellent computational speed (8 s). The results from the '0.5&1.0 mm grids' setting improved the accuracy compared to the use of '1.0 mm grid' alone, showing comparable accuracy to that of '0.5 mm grid'. The computation speed in this case was compatible for semi real-time user feedback (30 s). For these reasons, we concluded that the multi-resolution analysis approach allowed for a faster simulation with a minimal fidelity loss. We note that, although we used a combination of only two levels of resolution grids in the present work, more than two levels can be employed to cover a greater volume. The use of a time-variant adaptive discretization method (called as 're-meshing technique') (Bouchard *et al.*, 2000) can also be considered to flexibly allocate the localized grid settings to track the location of acoustic wave front while the simulation is running.

The simulation time period used in this study was 60 μs, which was enough to characterize the initial propagation to the focal point in space (our actual measurement was done covering a 100 μs time period). The use of longer sonication duration (TBD = 10 ms) did not affect the actual measurement, suggesting the choice of the period for the simulation was appropriate for our experimental setting in the open skull configuration. However, the use of short simulation time may not adequately characterize the acoustic profiles resulting from the steady-state wave propagations inside of the closed cranium (such as reverberations (Younan *et al.*, 2013) or the formation of the standing wave in human and primate skulls (Deffieux and Konofagou, 2010)). Indeed, based on our simulation on a closed ovine skull using a longer simulation time, we observed presence of reverberations and standing wave formation near the floor of the skull (figure 7). In addition, we note that the use of '0.5&1.0 mm grids' showed improved simulation speed while retaining the accuracy, compared to the other multi-resolution settings (*i.e.,* '0.5&2.0 mm grids' and '1.0&2.0 mm grids'). In conjunction with the findings from *ex vivo* skull simulations (open-skull configurations), our findings confirm the computational efficacy of the multi-resolution approach for later *in vivo* applications.

Performing a simulation using a closed skull is ideal; however, hydrophone measurements performed in a completely closed skull is a challenging task. Use of the higher acoustic intensity and non-invasive method such as ARFI (Kaye *et al.*, 2011) can be gainfully used to validate the simulation accuracy. The expansion of the simulation volume, for example, to cover the typical adult human head will inevitably increase the computation time, even using the multi-resolution approach. Figure 8 illustrates the two-level, multi-resolution grid settings adapted to simulate tFUS application in a human skull (Visible Human Project CT datasets (Ackerman, 1998)) as well as a sheep skull (settings are shown in table 6). In the human skull, assuming the same type of transducer used in the sheep application (*i.e.*, focal length 30 mm), the FUS focus is likely to be administered only to the cortical area. In this case, the number of nodes for the global grid is 6,300,000 (= 180 × 200 × 175, assigned as the field size) and 2,352,000 (= 140 × 140 × 120, *i.e.*, dotted box in the figure 8(b)) for the local grid. If we were to use a larger transducer (*e.g.*, 80 mm aperture) with greater focal

length (90 mm) for deep brain stimulation in humans (as conducted in Deffieux and Konofagou, 2010), the global grid nodes would remain the same (*i.e.*, 6,300,000), however, the local grid size must be expanded to include the larger transducer and greater focal length. Thus, it increases the number of local grid nodes to 6,480,000 (= 180 × 180 × 200, *i.e.*, dotted box in the figure 8(c)). Factoring in the increased number of time steps (6,000 steps, which is ~2.5 times greater than the simulation in a sheep skull; table 6) to reflect the size of the skull cavity in humans, the computational time will increase ~5 times (150 s) for the case of the cortical stimulation and ~7.5 times (225 s) for the case of deep brain stimulation. These approximations leave a margin of improvement for reducing the computation time by optimizing the simulation parameters through multiple levels of resolution grids. Employing a GPU device with higher processing capability (in both speed and parallel threading) can also be helpful to further alleviate the concerns over the computational time. Application of the technique in humans and its detailed quantitative evaluation constitute subjects for further investigation.

The developed simulation method aims to provide the operator with information regarding the estimated position, shape, and pressure level of the focus with respect to the position of the FUS transducer. However, the manual maneuvering of the transducer in space is still subject to inadvertent human error. The adoption of the inverse analysis techniques (Rekanos, 2002; Abenius and Strand, 2006) can be used to automatically identify the optimal position/orientation of the transducer with respect to the head. The technique, when combined with a robotic transducer positioning system (Kim and Lee, 2016), will be conducive to delivering the desired pressure level of sonication to the region-of-interest with minimal human intervention.

## 5. Conclusion

A multi-resolution approach, designed for simulating transcranial acoustic propagation from a single-element transducer, was implemented and evaluated in an ovine skull model. The flexibility of assigning different combinations of resolution grids, combined with the use of a GPU-based parallel computation environment, allowed for achieving simulation accuracy while greatly improving the computation speed. The approach is capable of providing on-site feedback information to the operator regarding the location and pressure amplitude of the acoustic focus. The extension and evaluation of the method in a human setting are needed to promote safety and efficacy of tFUS-mediated brain stimulation for neuroscientific research and therapeutic applications.

## Supplementary Material

Refer to Web version on PubMed Central for supplementary material.

## Acknowledgments

This study was supported by NIH (RO1 MH111763, to S.S. Yoo). We would like to thank Dr. Yongzhi Zhang and Ms. Lori Foley for the skull extraction, and Dr. Nathan J. McDannold for the initial consultation regarding the project.

## References


Abenius E, Strand B. Solving inverse electromagnetic problems using FDTD and gradient-based minimization. Int J Numer Methods Eng. 2006; 68:650–73.

Ackerman MJ. The visible human project. Proc IEEE. 1998; 86:504–11.

Ala G, Francomano E, Tortorici A, Toscano E, Viola F. A smoothed particle interpolation scheme for transient electromagnetic simulation. IEEE Trans Magn. 2006; 42:647–50.

Aubry JF, Tanter M, Pernot M, Thosmas JL, Fink M. Experimental demonstration of noninvasive transskull adaptive focusing based on prior computed tomography scans. J Acoust Soc Am. 2003; 113:84–93. [PubMed: 12558249]

Bailey M, Cunitz B, Dunmire B, Paun M, Lee F, Ross S, Lingeman J, Coburn M, Wessells H, Sorensen M, Harper J. Ultrasonic propulsion of kidney stones: preliminary results of human feasibility study. IEEE Int Ultrason Symp. 2014:511–4. [PubMed: 26203347]

Baron C, Aubry JF, Tanter M, Meairs S, Fink M. Simulation of intracranial acoustic fields in clinical trials of sonothrombolysis. Ultrasound Med Biol. 2009; 35:1148–58. [PubMed: 19394756]

Bathe, KJ. Finite element procedures. Klaus-Jurgen Bathe; 2006.

Bouchard PO, Bay F, Chastel Y, Tovena I. Crack propagation modelling using an advanced remeshing technique. Comput Meth Appl Mech Eng. 2000; 189:723–42.

Burger, W., Burge, MJ. Principles of digital image processing. Springer; 2009.

Chauvet D, Marsac L, Pernot M, Boch AL, Guillevin R, Salameh N, Souris L, Darrasse L, Fink M, Tanter M, Aubry JF. Targeting accuracy of transcranial magnetic resonance-guided high-intensity focused ultrasound brain therapy: a fresh cadaver model. J Neurosurg. 2013; 118:1046–52. [PubMed: 23451909]

Clement GT, White PJ, King RL, McDannold N, Hynynen K. A magnetic resonance imaging-compatible, large-scale array for trans-skull ultrasound surgery and therapy. J Ultrasound Med. 2005; 24:1117–25. [PubMed: 16040827]

Coluccia D, Fandino J, Schwyzer L, O'Gorman R, Remonda L, Anon J, Martin E, Werner B. First noninvasive thermal ablation of a brain tumor with MR-guided focused ultrasound. J Ther Ultrasound. 2014; 2:17. [PubMed: 25671132]

Comsol. COMSOL multiphysics user's guide. 2005. Version: September

Deffieux T, Konofagou EE. Numerical study of a simple transcranial focused ultrasound system applied to blood-brain barrier opening. IEEE Trans Ultrason Ferroelectr Freq Control. 2010; 57:2637–53. [PubMed: 21156360]

Deffieux T, Younan Y, Wattiez N, Tanter M, Pouget P, Aubry JF. Low-intensity focused ultrasound modulates monkey visuomotor behavior. Curr Biol. 2013; 23:2430–3. [PubMed: 24239121]

Downs ME, Buch A, Sierra C, Karakatsani ME, Teichert T, Chen S, Konofagou EE, Ferrera VP. Long-term safety of repeated blood-brain barrier opening via focused ultrasound with microbubbles in non-human primates performing a cognitive task. PLoS One. 2015; 10:e0125911. [PubMed: 25945493]

Elias WJ, Huss D, Voss T, Loomba J, Khaled M, Zadicario E, Frysinger RC, Sperling SA, Wylie S, Monteith SJ, Druzgal J, Shah BB, Harrison M, Wintermark M. A pilot study of focused ultrasound thalamotomy for essential tremor. N Engl J Med. 2013; 369:640–8. [PubMed: 23944301]

Evans JA, Tavakoli MB. Ultrasonic attenuation and velocity in bone. Phys Med Biol. 1990; 35:1387. [PubMed: 2243843]

Fellah ZE, Chapelon JY, Berger S, Lauriks W, Depollier C. Ultrasonic wave propagation in human cancellous bone: application of Biot theory. J Acoust Soc Am. 2004; 116:61–73. [PubMed: 15295965]

Fitzpatrick JM, West JB, Maurer CR Jr. Predicting error in rigid-body point-based registration. IEEE Trans Med Imaging. 1998; 17:694–702. [PubMed: 9874293]

Fry FJ, Barger JE. Acoustical properties of the human skull. J Acoust Soc Am. 1978; 63:1576–90. [PubMed: 690336]

Goss SA, Frizzell LA, Dunn F. Ultrasonic absorption and attenuation in mammalian tissues. Ultrasound Med Biol. 1979; 5:181–6. [PubMed: 556199]

Hosokawa A. Simulation of ultrasound propagation through bovine cancellous bone using elastic and Biot's finite-difference time-domain methods. J Acoust Soc Am. 2005; 118:1782–9. [PubMed: 16240836]

Hynynen K. Ultrasound for drug and gene delivery to the brain. Adv Drug Deliv Rev. 2008; 60:1209–17. [PubMed: 18486271]

Hynynen K, Clement GT, McDannold N, Vykhodtseva N, King R, White PJ, Vitek S, Jolesz FA. 500-element ultrasound phased array system for noninvasive focal surgery of the brain: a preliminary rabbit study with ex vivo human skulls. Magn Reson Med. 2004; 52:100–7. [PubMed: 15236372]

Hynynen K, McDannold N, Vykhodtseva N, Raymond S, Weissleder R, Jolesz FA, Sheikov N. Focal disruption of the blood-brain barrier due to 260-kHz ultrasound bursts: a method for molecular imaging and targeted drug delivery. J Neurosurg. 2006; 105:445–54. [PubMed: 16961141]

Hynynen K, Pomeroy O, Smith DN, Huber PE, McDannold NJ, Kettenbach J, Baum J, Singer S, Jolesz FA. MR imaging-guided focused ultrasound surgery of fibroadenomas in the breast: a feasibility study. Radiology. 2001; 219:176–85. [PubMed: 11274554]

Ishihara Y, Calderon A, Watanabe H, Okamoto K, Suzuki Y, Kuroda K, Suzuki Y. A precise and fast temperature mapping using water proton chemical shift. Magn Reson Med. 1995; 34:814–23. [PubMed: 8598808]

Jiang H, Arai H. 3D FDTD analysis by using non-uniform mesh. Proc IEEE ICMMT. 1998:947–950.

Jing Y, Meral FC, Clement GT. Time-reversal transcranial ultrasound beam focusing using a k-space method. Phys Med Biol. 2012; 57:901–17. [PubMed: 22290477]

Jing Y, Shen D, Clement GT. Verification of the Westervelt equation for focused transducers. IEEE Trans Ultrason Ferroelectr Freq Control. 2011; 58:1097–101. [PubMed: 21622065]

Kaufman JJ, Luo G, Siffert RS. Ultrasound simulation in bone. IEEE Trans Ultrason Ferroelectr Freq Control. 2008; 55:1205–18. [PubMed: 18599409]

Kaye EA, Chen J, Pauly KB. Rapid MR-ARFI method for focal spot localization during focused ultrasound therapy. Magn Reson Med. 2011; 65:738–43. [PubMed: 21337406]

Kennedy JE. High-intensity focused ultrasound in the treatment of solid tumours. Nat Rev Cancer. 2005; 5:321–7. [PubMed: 15776004]

Kim H, Chiu A, Lee SD, Fischer K, Yoo SS. Focused ultrasound-mediated non-invasive brain stimulation: examination of sonication parameters. Brain Stimul. 2014; 7:748–56. [PubMed: 25088462]

Kim H, Chiu A, Park S, Yoo SS. Image-guided navigation of single-element focused ultrasound transducer. Int J Imaging Syst Technol. 2012a; 22:177–84. [PubMed: 25232203]

Kim H, Lee SD, Chiu A, Yoo SS, Park S. Estimation of the spatial profile of neuromodulation and the tempral latency in motor responses induced by focused ultrasound brain stimulation. Neuroreport. 2014; 25:475–9. [PubMed: 24384503]

Kim H, Park MA, Wang S, Chiu A, Fischer K, Yoo SS. PET/CT imaging evidence of FUS-mediated (18)F-FDG uptake changes in rat brain. Med Phys. 2013; 40:033501. [PubMed: 23464343]

Kim H, Park MY, Lee SD, Lee W, Chiu A, Yoo SS. Suppression of EEG visual-evoked potentials in rats through neuromodulatory focused ultrasound. Neuroreport. 2015; 26:211–5. [PubMed: 25646585]

Kim H, Taghados SJ, Fischer K, Maeng LS, Park S, Yoo SS. Noninvasive transcranial stimulation of rat abducens nerve by focused ultrasound. Ultrasound Med Biol. 2012b; 38:1568–75. [PubMed: 22763009]

Kim J, Lee S. Development of a wearable robotic positioning system for noninvasive transcranial focused ultrasound stimulation. IEEE ASME Trans Mechatron. 2016; 21:2284–93.

Konofagou E, Thierman J, Hynynen K. A focused ultrasound method for simultaneous diagnostic and therapeutic applications—A simulation study. Phys Med Biol. 2001; 46:2967–84. [PubMed: 11720358]

Krumpholz M, Katehi LP. MRTD: New time-domain schemes based on multiresolution analysis. IEEE Trans Microw Theory Techn. 1996; 44:555–71.

Kurtz C, Stumpf A, Malet J-P, Gançarski P, Puissant A, Passat N. Hierarchical extraction of landslides from multiresolution remotely sensed optical images. J Photogramm Remote Sens. 2014; 87:122–36.

Kyriakou A, Neufeld E, Werner B, Szekely G, Kuster N. Full-wave acoustic and thermal modeling of transcranial ultrasound propagation and investigation of skull-induced aberration correction techniques: a feasibility study. J Ther Ultrasound. 2015; 3:11. [PubMed: 26236478]

Lee KI, Hughes ER, Humphrey VF, Leighton TG, Choi MJ. Empirical angle-dependent Biot and MBA models for acoustic anisotropy in cancellous bone. Phys Med Biol. 2007; 52:59–73. [PubMed: 17183128]

Lee W, Chung YA, Jung Y, Song IU, Yoo SS. Simultaneous acoustic stimulation of human primary and secondary somatosensory cortices using transcranial focused ultrasound. BMC Neurosci. 2016a; 17:68. [PubMed: 27784293]

Lee W, Kim H, Jung Y, Song IU, Chung YA, Yoo SS. Image-guided transcranial focused ultrasound stimulates human primary somatosensory cortex. Sci Rep. 2015; 5:8743. [PubMed: 25735418]

Lee W, Kim HC, Jung Y, Chung YA, Song IU, Lee JH, Yoo SS. Transcranial focused ultrasound stimulation of human primary visual cortex. Sci Rep. 2016b; 6:34026. [PubMed: 27658372]

Lee W, Kim S, Kim B, Lee C, Chung YA, Kim L, Yoo SS. Non-invasive transmission of sensorimotor information in humans using an EEG/focused ultrasound brain-to-brain interface. PLoS One. 2017; 12:e0178476. [PubMed: 28598972]

Lee W, Lee SD, Park MY, Foley L, Purcell-Estabrook E, Kim H, Fischer K, Maeng LS, Yoo SS. Image-guided focused ultrasound-mediated regional brain stimulation in sheep. Ultrasound Med Biol. 2016c; 42:459–70. [PubMed: 26525652]

Legon W, Sato TF, Opitz A, Mueller J, Barbour A, Williams A, Tyler WJ. Transcranial focused ultrasound modulates the activity of primary somatosensory cortex in humans. Nat Neurosci. 2014; 17:322–9. [PubMed: 24413698]

Liebler M, Ginter S, Dreyer T, Riedlinger RE. Full wave modeling of therapeutic ultrasound: efficient time-domain implementation of the frequency power-law attenuation. J Acoust Soc Am. 2004; 116:2742–50. [PubMed: 15603120]

Lighthill J. Acoustic streaming. J Sound Vib. 1978; 61:391–418.

Liu, GR., Liu, MB. Smoothed particle hydrodynamics: a meshfree particle method. World Scientific; 2003.

Liu HL, Chang H, Chen WS, Shih TC, Hsiao JK, Lin WL. Feasibility of transrib focused ultrasound thermal ablation for liver tumors using a spherically curved 2D array: a numerical study. Med Phys. 2007; 34:3436–48. [PubMed: 17926945]

Madersbacher S, Marberger M. High-energy shockwaves and extracorporeal high-intensity focused ultrasound. J Endourol. 2003; 17:667–72. [PubMed: 14622487]

Marquet F, Pernot M, Aubry JF, Montaldo G, Marsac L, Tanter M, Fink M. Non-invasive transcranial ultrasound therapy based on a 3D CT scan: protocol validation and in vitro results. Phys Med Biol. 2009; 54:2597–613. [PubMed: 19351986]

Martin E, Jeanmonod D, Morel A, Zadicario E, Werner B. High-intensity focused ultrasound for noninvasive functional neurosurgery. Ann Neurol. 2009; 66:858–61. [PubMed: 20033983]

Martin E, Ling YT, Treeby BE. Simulating focused ultrasound transducers using discrete sources on regular cartesian grids. IEEE Trans Ultrason Ferroelectr Freq Control. 2016; 63:1535–42. [PubMed: 27541793]

McDannold N, Tempany Clare, Fennessy F, So MJ, Rybicki F, Stewart E, Jolesz F, Hynynen K. Uterine leiomyomas: MR imaging-based thermometry and thermal dosimetry during focused ultrasound thermal ablation. Radiology. 2006; 240:263–72. [PubMed: 16793983]

McDannold N, Clement GT, Black P, Jolesz F, Hynynen K. Transcranial magnetic resonance imaging-guided focused ultrasound surgery of brain tumors: initial findings in 3 patients. Neurosurgery. 2010; 66:323–32. [PubMed: 20087132]

McDannold N, Hynynen K, Wolf D, Wolf G, Jolesz F. MRI evaluation of thermal ablation of tumors with focused ultrasound. J Magn Reson Imaging. 1998; 8:91–100. [PubMed: 9500266]

McDannold N, Vykhodtseva N, Hynynen K. Blood-brain barrier disruption induced by focused ultrasound and circulating preformed microbubbles appears to be characterized by the mechanical index. Ultrasound Med Biol. 2008; 34:834–40. [PubMed: 18207311]

McDannold N, Zhang Y, Vykhodtseva N. Blood-brain barrier disruption and vascular damage induced by ultrasound bursts combined with microbubbles can be influenced by choice of anesthesia protocol. Ultrasound Med Biol. 2011; 37:1259–70. [PubMed: 21645965]

Moghari MH, Abolmaesumi P. Point-based rigid-body registration using an unscented kalman filter. IEEE Trans Med Imag. 2007; 26:1708–28.

Mueller JK, Ai L, Bansal P, Legon W. Numerical evaluation of the skull for human neuromodulation with transcranial focused ultrasound. J Neural Eng. 2017; 14:066012. [PubMed: 28777075]

Namiki T. 3-D ADI-FDTD method-unconditionally stable time-domain algorithm for solving full vector Maxwell's equations. IEEE Trans Microw Theory Tech. 2000; 48:1743–8.

Noh G, Bathe KJ. An explicit time integration scheme for the analysis of wave propagations. Comput Strut. 2013; 129:178–93.

Pietrzyk U, Herholz K, Fink G, Jacobs A, Mielke R, Slansky I, Wurker M, Heiss WD. An interactive technique for three-dimensional image registration: validation for PET, SPECT, MRI and CT brain studies. J Nucl Med. 1994; 35:2011–8. [PubMed: 7989986]

Pinton GF, Dahl J, Rosenzweig S, Trahey GE. A heterogeneous nonlinear attenuating full-wave model of ultrasound. IEEE Trans Ultrason Ferroelectr Freq Control. 2009; 56:474–88. [PubMed: 19411208]

Pinton GF, Aubry JF, Bossy E, Muller M, Pernot M, Tanter M. Attenuation, scattering and absorption of ultrasound in the skull bone. Med Phys. 2012; 39:299–307. [PubMed: 22225300]

Pulkkinen A, Werner B, Martin E, Hynynen K. Numerical simulations of clinical focused ultrasound functional neurosurgery. Phys Med Biol. 2014; 59:1679–700. [PubMed: 24619067]

Rekanos IT. Inverse scattering in the time domain: An iterative method using an FDTD sensitivity analysis scheme. IEEE Trans Magn. 2002; 38:1117–20.

Robertson J, Martin E, Cox B, Treeby BE. Sensitivity of simulated transcranial ultrasound fields to acoustic medium property maps. Phys Med Biol. 2017a; 62:2559–80. [PubMed: 28165334]

Robertson JL, Cox BT, Jaros J, Treeby BE. Accurate simulation of transcranial ultrasound propagation for ultrasonic neuromodulation and stimulation. J Acoust Soc Am. 2017b; 141:1726–38. [PubMed: 28372121]

Schwenke M, Strehlow J, Haase S, Jenne J, Tanner C, Lango T, Loeve AJ, Karakitsios I, Xiao X, Levy Y, Sat G, Bezzi M, Braunewell S, Guenther M, Melzer A, Preusser T. An integrated model-based software for FUS in moving abdominal organs. Int J Hyperthermia. 2015; 31:240–50. [PubMed: 25786982]

Sheen, S., Chien, H., Raptis, A. Ultrasonic methods for measuring liquid viscosity and volume percent of solids. Argonne National Lab; IL (United States): 1997.

Sheikov N, McDannold N, Vykhodtseva N, Jolesz F, Hynynen K. Cellular mechanisms of the blood-brain barrier opening induced by ultrasound in presence of microbubbles. Ultrasound Med Biol. 2004; 30:979–89. [PubMed: 15313330]

Solovchuk M, Sheu TW, Thiriet M. Simulation of nonlinear Westervelt equation for the investigation of acoustic streaming and nonlinear propagation effects. J Acoust Soc Am. 2013; 134:3931–42. [PubMed: 24180802]

Taflove, A., Hagness, SC. Computational electrodynamics: the finite-difference time-domain method. Artech house; 2005.

Treeby BE, Cox BT. k-Wave: MATLAB toolbox for the simulation and reconstruction of photoacoustic wave fields. J Biomed Opt. 2010; 15:021314–12. [PubMed: 20459236]

Tung YS, Liu HL, Wu CC, Ju KC, Chen WS, Lin WL. Contrast-agent-enhanced ultrasound thermal ablation. Ultrasound Med Biol. 2006; 32:1103–10. [PubMed: 16829324]

van Lier OR, Fournier RA, Bradley RL, Thiffault N. A multi-resolution satellite imagery approach for large area mapping of ericaceous shrubs in Northern Quebec, Canada. Int J Appl Earth Obs Geoinf. 2009; 11:334–43.

Wattiez N, Constans C, Deffieux T, Daye PM, Tanter M, Aubry JF, Pouget P. Transcranial ultrasonic stimulation modulates single-neuron discharge in macaques performing an antisaccade task. Brain Stimul. 2017; 10:1024–31. [PubMed: 28789857]

West JB, Maurer CR Jr. Designing optically tracked instruments for image-guided surgery. IEEE Trans Med Imaging. 2004; 23:533–45. [PubMed: 15147007]

Westervelt PJ. Scattering of sound by sound. J Acoust Soc Am. 1957; 29:199–203.

White PJ, Clement GT, Hynynen K. Longitudinal and shear mode ultrasound propagation in human skull bone. Ultrasound Med Biol. 2006; 32:1085–96. [PubMed: 16829322]

Yin X, Hynynen K. A numerical study of transcranial focused ultrasound beam propagation at low frequency. Phys Med Biol. 2005; 50:1821–36. [PubMed: 15815098]

Yoo SS, Bystritsky A, Lee JH, Zhang Y, Fischer K, Min BK, McDannold NJ, Pascual-Leone A, Jolesz FA. Focused ultrasound modulates region-specific brain activity. Neuroimage. 2011; 56:1267–75. [PubMed: 21354315]

Yoo SS, Guttmann CR, Panych LP. Multiresolution data acquisition and detection in functional MRI. Neuroimage. 2001; 14:1476–85. [PubMed: 11707104]

Yoo SS, Guttmann CR, Zhao L, Panych LP. Real-time adaptive functional MRI. Neuroimage. 1999; 10:596–606. [PubMed: 10547337]

Yoo SS, Yoon K, Croce P, Cammalleri A, Margolin RW, Lee W. Focused ultrasound brain stimulation to anesthetized rats induces long-term changes in somatosensory evoked potentials. Int J Imaging Syst Technol. 2018 In press.

Younan Y, Deffieux T, Larrat B, Fink M, Tanter M, Aubry JF. Influence of the pressure field distribution in transcranial ultrasonic neurostimulation. Med Phys. 2013; 40:082902. [PubMed: 23927357]

Yu Y, Chen Z. A 3-D radial point interpolation method for meshless time-domain modeling. IEEE Trans Microw Theory Techn. 2009; 57:2015–20.

Zhi ZH, Xu X, Jing L. An effective finite difference method for simulation of bioheat transfer in irregular tissues. J Heat Transfer. 2013; 135:071003.

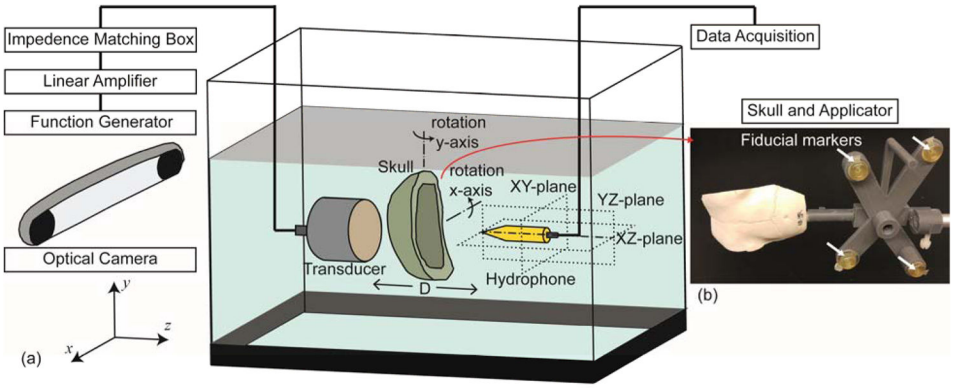


**Figure 1.**

(a) Schematic of the acoustic field measurement setup in the actual space (not drawn to scale). The transducer was actuated by an electrical signal generated and amplified by a function generator and a linear amplifier, respectively, with impedance matching. Hydrophone scanning was conducted in YZ-, XZ-, XY-planes, and the skull was rotated along each of the *x* and *y* axis (0°, ±10° and ±15°). (b) An example of a sheep skull with an applicator. The actual location and orientation of the skull was obtained by an optical tracking system and co-registered to the skull CT data using the coordinate information of the corresponding four fiducial markers indicated with white arrows.

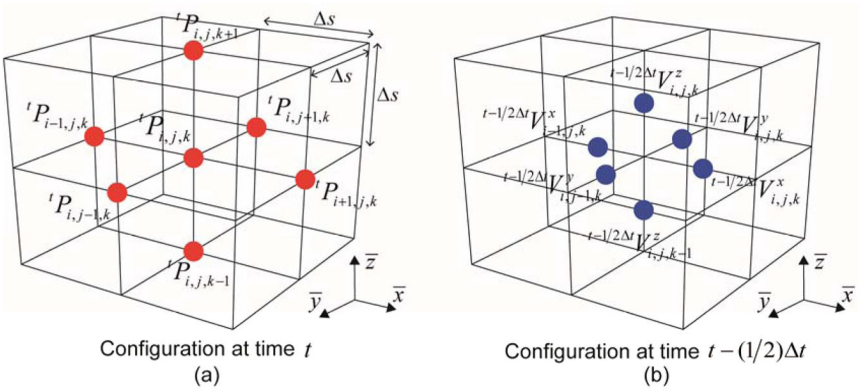


**Figure 2.**

The graphical illustration of the staggered grids (solid lines) and the corresponding pressure and velocity nodes (dots). (a) The pressure grid and nodes at time $t$ and (b) the velocity grid and node set-up at time $t-(1/2)\Delta t$.

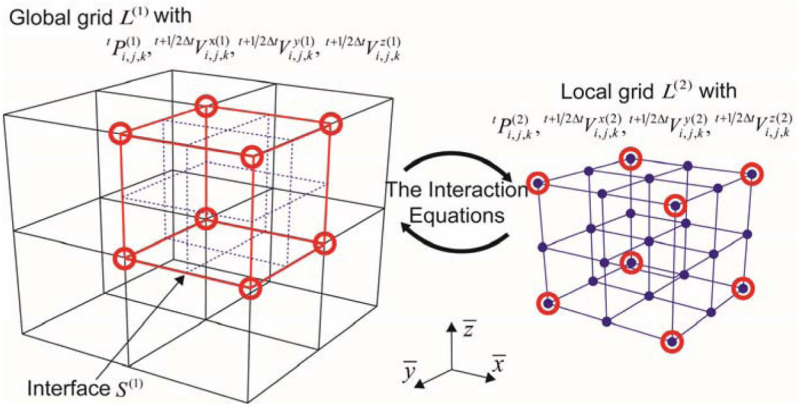


**Figure 3.**

Conceptual description of multi-resolution grids approach. The red circles (nodal points) and red lines (interface) represent the key interactions where equations (6) and (7) were used to interconnect the grids of differing resolutions.

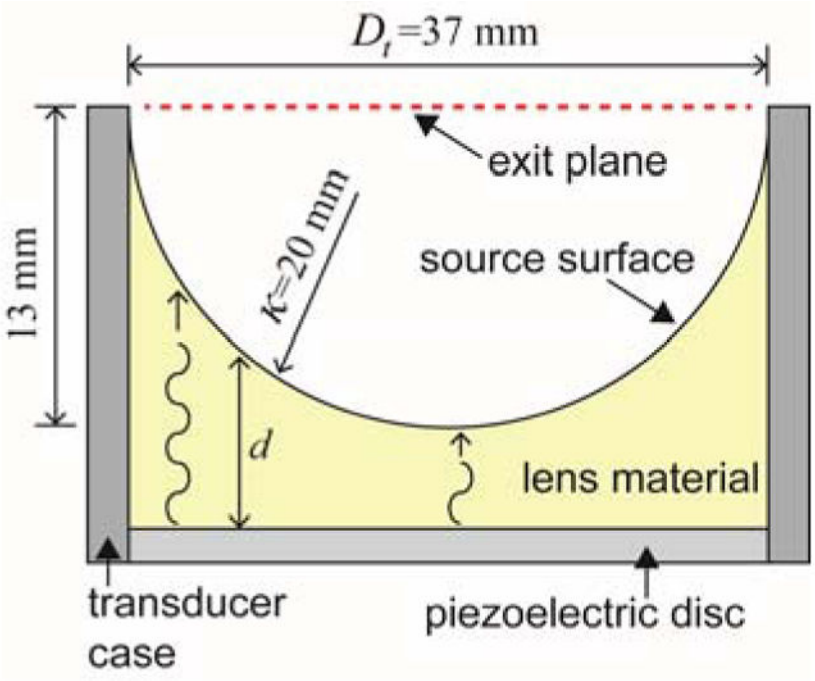


**Figure 4.**

Dimensions and composition of FUS transducer used. The concave lens material focuses the ultrasound waves generated from the piezoelectric disc. $\kappa$ is the radius of the concave lens (20 mm), and $d$ is wave travel distance in the lens material. $D_t$ indicates the diameter of the transducer opening at the exit plane.

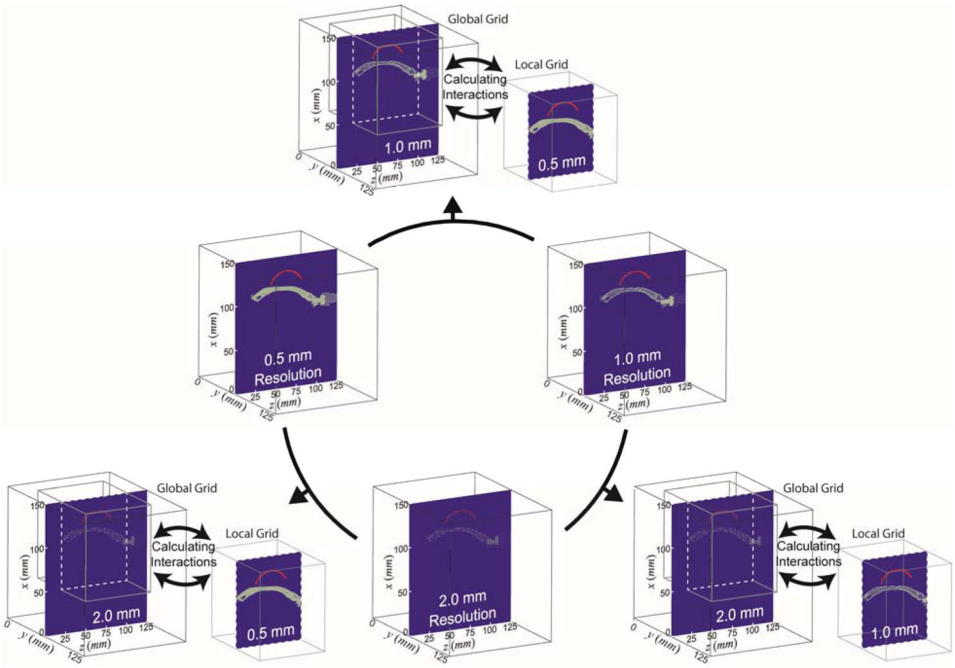


**Figure 5.**

Schematics of the grid settings for the implemented acoustic simulation. The fixed-resolution simulations were performed with various resolution settings of ‘0.5 mm grid’ (left, middle row), ‘1.0 mm grid’ (right, middle row), and ‘2.0 mm grid’ (middle, bottom row). The multi-resolution simulations were performed using the combination of two resolution settings (‘0.5&1.0 mm grids’, ‘0.5&2.0 mm grids’, and ‘1.0&2.0 mm grids’). The higher resolution setting was assigned to the local grid. On the blue-colored planes, red-colored profiles depict the acoustic source surface profile of the FUS transducer and the gray dots (conveying the information on resolutions) delineate the skull profile.

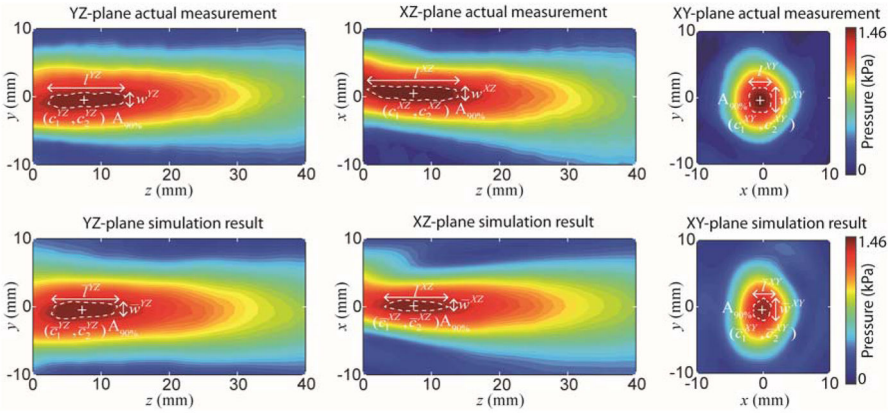


**Figure 6.**

An example of acoustic pressure distribution on the YZ-, XZ-, XY-plane (from left to right columns) from the actual measurement (top row) and the simulation results (bottom row) obtained from a skull phantom (‘S3’, at y+15° configuration). The resolution setting of ‘0.5 mm grid’ was used. ‘+’ denotes the center of the focus. The white dashed line indicates the region of $A_{90\%}$.

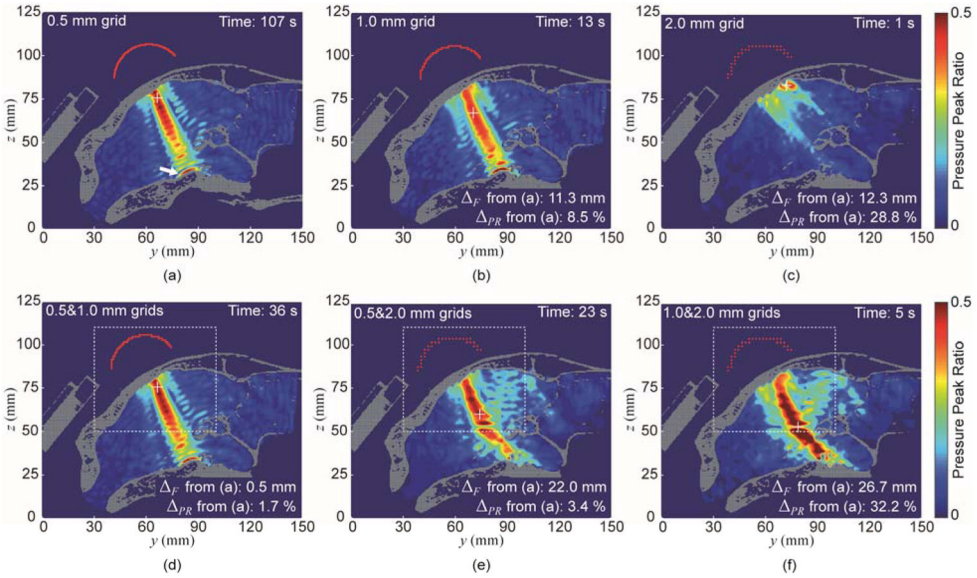


**Figure 7.**

The simulation results of acoustic pressure distribution on the sagittal plane obtained from (a) ‘0.5 mm grid’, (b) ‘1.0 mm grid’, (c) ‘2.0 mm grid’, (d) ‘0.5&1.0 mm grid’, (e) ‘0.5&2.0 mm grid’, and (f) ‘1.0&2.0 mm grid’. ‘+’ denotes the location of the maximum pressure value. The pressure level inside the skull was pseudo-colored, being scaled with reference to the peak pressure value obtained in the absence of the skull, to represent the pressure peak ratio $R^{YZ}$. The white dashed line indicates the region of the local grid.

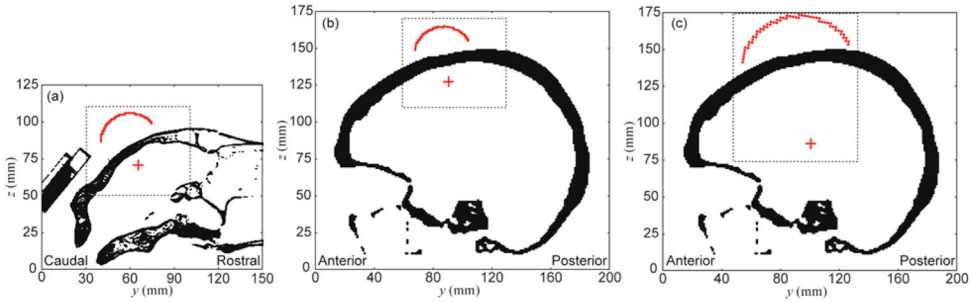


**Figure 8.**

Global (entire field-of-view) and local grid settings (dotted rectangular area) for the multi-resolution approach illustrated in sheep and human skull models (shown on the sagittal plane using the same spatial scale). The profile of the transducer surface is outlined in red while the estimated focal location is denoted as a red crosshair. A uniform spatial scale was used across all figures for their size comparisons. (a) The sheep skull model showing 100 × 150 × 125 global (at 1 mm resolution) and 140 × 140 × 120 local grids (at 0.5 mm resolution), (b) an example of human skull model for cortical area stimulation with 180 × 200 × 175 global (at 1 mm resolution) and 140 × 140 × 120 local grids (at 0.5 mm resolution), and (c) an example of human skull model for deep brain stimulation with 180 × 200 × 175 global (at 1 mm resolution) and 180 × 180 × 200 local grids (at 0.5 mm resolution).

**Table 1**

Detailed description of the virtual simulation space. The simulations on ‘0.5 mm grid’, ‘1.0 mm grid’ and ‘2.0 mm grid’ were performed using fixed resolution grids. ‘0.5&1.0 mm grids’, ‘0.5&2.0 mm grids’ and ‘1.0&2.0 mm grids’ denote the simulation conducted using multi-resolution grids. All represented in isotropic voxels.

| Grid Settings | | Resolution (mm) | Number of Matrices | Number of Nodes | Physical Field Size ($mm^3$) | Discretized Time Interval (μs) | Number of Time Steps |
|---|---|---|---|---|---|---|---|
| Fixed-resolution | | | | | | | |
| 0.5 mm | Fixed | 0.5 | 300 × 250 × 250 | 18,750,000 | 150 × 125 × 125 | 0.05 | 1,200 |
| 1.0 mm | Fixed | 1.0 | 150 × 125 × 125 | 2,343,750 | 150 × 125 × 125 | 0.05 | 1,200 |
| 2.0 mm | Fixed | 2.0 | 75 × 62 × 62 | 288,300 | 150 × 124 × 124 | 0.05 | 1,200 |
| Multi-resolution | | | | | | | |
| 0.5&1.0 mm | Global | 1.0 | 150 × 125 × 125 | 2,343,750 | 150 × 125 × 125 | 0.05 | 1,200 |
| | Local | 0.5 | 201 × 151 × 151 | 4,583,001 | | | |
| 0.5&2.0 mm | Global | 2.0 | 75 × 62 × 62 | 288,300 | 150 × 124 × 124 | 0.05 | 1,200 |
| | Local | 0.5 | 201 × 153 × 153 | 4,705,209 | | | |
| 1.0&2.0 mm | Global | 2.0 | 75 × 62 × 62 | 288,300 | 150 × 124 × 124 | 0.05 | 1,200 |
| | Local | 1.0 | 101 × 77 × 77 | 598,829 | | | |

**Table 2**

Detailed description of the simulation space for the closed skull. The simulations on ‘0.5 mm grid’, ‘1.0 mm grid’ and ‘2.0 mm grid’ were performed using fixed resolution grids. ‘0.5&1.0 mm grids’, ‘0.5&2.0 mm grids’ and ‘1.0&2.0 mm grids’ denote the simulation conducted using multi-resolution grids. All represented in isotropic voxels.

| Grid Settings | | Resolution (mm) | Number of Matrices | Number of Nodes | Physical Field Size ($mm^3$) | Discretized Time Interval (μs) | Number of Time Steps |
|---|---|---|---|---|---|---|---|
| Fixed-resolution | | | | | | | |
| 0.5 mm | Fixed | 0.5 | 200 × 300 × 250 | 15,000,000 | 100 × 150 × 125 | 0.05 | 2,400 |
| 1.0 mm | Fixed | 1.0 | 100 × 150 × 125 | 1,875,000 | 100 × 150 × 125 | 0.05 | 2,400 |
| 2.0 mm | Fixed | 2.0 | 50 × 75 × 62 | 232,500 | 100 × 150 × 124 | 0.05 | 2,400 |
| Multi-resolution | | | | | | | |
| 0.5&1.0 mm | Global | 1.0 | 100 × 150 × 125 | 1,875,000 | 100 × 150 × 125 | 0.05 | 2,400 |
| | Local | 0.5 | 140 × 140 × 120 | 2,352,000 | | | |
| 0.5&2.0 mm | Global | 2.0 | 50 × 75 × 62 | 232,500 | 100 × 150 × 124 | 0.05 | 2,400 |
| | Local | 0.5 | 140 × 140 × 120 | 2,352,000 | | | |
| 1.0&2.0 mm | Global | 2.0 | 50 × 75 × 62 | 232,500 | 100 × 150 × 124 | 0.05 | 2,400 |
| | Local | 1.0 | 70 × 70 × 60 | 294,000 | | | |

## Table 3

The comparisons for simulation performance among different conditions of the skull processing and incident sonication angles. Case A was performed using processed skulls for all angles ($n$ = 2 sheep × 9 angles; 0°, x ±10°, x±15°, y±10°, y±15°). Case B was conducted using intact skulls for all angles ($n$ = 3 sheep × 9 angles; 0°, x±10°, x±15°, y±10°, y±15°). Case C was done using intact skulls with restricted angles ($n$ = 3 sheep × 5 angles; 0°, x±10° and y±10°).

| | **Simulation Conditions** | | |
|---|---|---|---|
| | **Case A*** | **Case B** | **Case C** |
| **Measurement Plane** | **Focal Position $\Delta_F$ (mm)** | | |
| YZ | 3.7 ± 2.1 | 1.6 ± 1.0 | 1.4 ± 0.9 |
| XZ | 4.4 ± 2.5 | 1.3 ± 0.7 | 1.2 ± 0.6 |
| XY | 2.7 ± 0.9 | 1.4 ± 0.6 | 1.4 ± 0.7 |
| | **Focal Dimension (mm)** | | |
| | Length $\Delta_l$ | | |
| YZ | 4.4 ± 2.7 | 2.3 ± 2.0 | 2.2 ± 1.7 |
| XZ | 5.5 ± 4.3 | 2.7 ± 1.8 | 2.2 ± 1.2 |
| XY | 0.8 ± 0.9 | 0.5 ± 0.5 | 0.5 ± 0.5 |
| | Width $\Delta_w$ | | |
| YZ | 1.0 ± 0.6 | 0.7 ± 0.5 | 0.7 ± 0.5 |
| XZ | 1.2 ± 1.6 | 0.8 ± 0.5 | 0.7 ± 0.5 |
| XY | 0.9 ± 0.8 | 0.6 ± 0.6 | 0.6 ± 0.5 |
| | **Peak Pressure $\Delta_{PR}$ (%)** | | |
| YZ | 9.9 ± 5.2 | 5.9 ± 6.2 | 4.9 ± 4.3 |
| XZ | 10.1 ± 6.0 | 6.3 ± 6.5 | 4.1 ± 3.4 |
| XY | 8.3 ± 6.6 | 5.2 ± 6.4 | 3.1 ± 3.2 |

* Note that segmentation and rescaling of CT image intensity was applied to Case A.

**Table 4**

The comparisons among various resolution grids used in simulation and its computational time.

| Measurement Plane | Fixed-resolution grid | | | Multi-resolution grids | | |
|---|---|---|---|---|---|---|
| | 0.5 mm | 1.0 mm | 2.0 mm | 0.5&1.0 mm | 0.5&2.0 mm | 1.0&2.0 mm |
| **Focal Position $\Delta_F$ (mm)** | | | | | | |
| YZ | 1.4 ± 0.9 | 2.4 ± 1.1 | 7.8 ± 0.7 | 1.5 ± 1.1 | 1.5 ± 1.0 | 2.3 ± 1.1 |
| XZ | 1.2 ± 0.6 | 1.7 ± 0.7 | 7.8 ± 1.7 | 1.3 ± 0.7 | 1.1 ± 0.6 | 1.7 ± 0.6 |
| XY | 1.4 ± 0.7 | 2.2 ± 1.0 | 8.9 ± 3.6 | 1.5 ± 0.6 | 1.4 ± 1.0 | 2.2 ± 1.0 |
| **Focal Dimension (mm)** | | | | | | |
| Length $\Delta_l$ | | | | | | |
| YZ | 2.2 ± 1.7 | 2.5 ± 1.9 | 14.6 ± 1.0 | 2.1 ± 1.9 | 2.3 ± 1.8 | 2.0 ± 1.7 |
| XZ | 2.2 ± 1.2 | 1.9 ± 0.9 | 14.5 ± 2.2 | 2.3 ± 1.2 | 2.7 ± 2.2 | 1.5 ± 1.4 |
| XY | 0.5 ± 0.5 | 0.8 ± 0.7 | 3.5 ± 4.5 | 0.3 ± 0.5 | 0.4 ± 0.6 | 0.9 ± 0.5 |
| Width $\Delta_w$ | | | | | | |
| YZ | 0.7 ± 0.5 | 0.8 ± 0.6 | 1.7 ± 3.0 | 0.6 ± 0.6 | 0.7 ± 0.6 | 0.6 ± 0.6 |
| XZ | 0.7 ± 0.5 | 0.3 ± 0.5 | 1.3 ± 1.2 | 0.7 ± 0.5 | 0.7 ± 0.5 | 0.4 ± 0.5 |
| XY | 0.6 ± 0.5 | 0.3 ± 0.5 | 4.5 ± 5.5 | 0.7 ± 0.5 | 0.5 ± 0.5 | 0.3 ± 0.5 |
| **Peak Pressure $\Delta_{PR}$ (%)** | | | | | | |
| YZ | 4.9 ± 4.3 | 6.8 ± 5.4 | 24.4 ± 10.4 | 5.4 ± 4.3 | 5.3 ± 2.5 | 7.1 ± 5.8 |
| XZ | 4.1 ± 3.4 | 6.9 ± 5.3 | 20.7 ± 12.4 | 4.2 ± 3.3 | 4.8 ± 4.4 | 7.5 ± 6.1 |
| XY | 3.1 ± 3.2 | 3.2 ± 3.0 | 47.7 ± 18.2 | 3.2 ± 2.8 | 4.5 ± 2.9 | 3.5 ± 2.9 |
| **Time (s)** | | | | | | |
| | 63 | 8 | 1 | 30 | 21 | 4 |

**Table 5**

The comparisons among various resolution grids used in a closed-skull simulation and its computational time.

| Fixed-resolution grid | | | Multi-resolution grids | | |
|---|---|---|---|---|---|
| **0.5 mm** | **1.0 mm** | **2.0 mm** | **0.5&1.0 mm** | **0.5&2.0 mm** | **1.0&2.0 mm** |
| **Focal Position $\Delta_F$ (mm)** | | | | | |
| Ref. * | 11.3 | 12.3 | 0.5 | 22.0 | 26.7 |
| **Peak Pressure $\Delta_{PR}$ (%)** | | | | | |
| Ref. * | 8.5 | 28.8 | 1.7 | 3.4 | 32.2 |
| **Time (s)** | | | | | |
| 107 | 13 | 1 | 36 | 23 | 5 |

* Reference value for comparison

**Table 6**

Comparisons among multi-resolution modeling of tFUS through sheep and human skulls. The local grid was assigned to model the space encompassing both transducer and the focal area.

| Model | | Resolution (mm) | Number of Matrices | Number of Nodes | Total Number of Nodes | Physical Field Size ($mm^3$) | Discretized Time Interval (μs) | Number of Time Steps | Estimated Computation Time (s) |
|---|---|---|---|---|---|---|---|---|---|
| Sheep Skull | Global | 1.0 | 100 × 150 × 125 | 1,875,000 | 4,227,000 | 100 × 150 × 125 | 0.05 | 2,400 | 30 |
| | Local | 0.5 | 140 × 140 × 120 | 2,352,000 | | | | | |
| Human Skull (Cortical) | Global | 1.0 | 180 × 200 × 175 | 6,300,000 | 8,652,000 | 180 × 200 × 175 | 0.05 | 6,000 | 150 |
| | Local | 0.5 | 140 × 140 × 120 | 2,352,000 | | | | | |
| Human Skull (Deep brain) | Global | 1.0 | 180 × 200 × 175 | 6,300,000 | 12,780,000 | 180 × 200 × 175 | 0.05 | 6,000 | 225 |
| | Local | 0.5 | 180 × 180 × 200 | 6,480,000 | | | | | |